THE JOURNAL OF PHYSICAL CHEMISTRY C

Article

Cite This: J. Phys. Chem. C 2019, 123, 17163−17169

pubs.acs.org/JPCC

Structure and Electrical Performance of $Na_2C_6O_6$ under High Pressure

Xuan Wang,[†] Peijie Zhang,[†] Xingyu Tang,[†] Junjie Guan,[†,‡] Xiaohuan Lin,[†] Yajie Wang,[†] Xiao Dong,[§] Binbin Yue,[†] Jinyuan Yan,[∥,⊥] Kuo Li,[*,†] Haiyan Zheng,[*,†] and Ho-kwang Mao[†,#]

[†]Center for High Pressure Science and Technology Advanced Research, Beijing 100094, P. R. China

[‡]School of Chemical Engineering and Technology, Tianjin University, Tianjin 300350, China

[§]Key Laboratory of Weak-Light Nonlinear Photonics, School of Physics, Nankai University, Tianjin 300071, China

[∥]Advanced Light Source, Lawrence Berkeley National Laboratory, Berkeley, California 94720, United States

[⊥]Earth and Planetary Sciences Department, University of California, Santa Cruz, California 95064, United States

[#]Geophysical Laboratory, Carnegie Institution of Washington, 5251 Broad Branch Road, NW, Washington, DC 20015, United States

Supporting Information

ABSTRACT: Sodium rhodizonate ($Na_2C_6O_6$) has very high theoretical capacity as a positive electrode material of sodium-ion batteries, but it still has problems such as low actual capacity and poor electronic/ionic conductivity. In order to improve its conductivity, we investigated its structure and electrical properties under high pressure. By performing in situ X-ray diffraction, Raman, infrared absorption, and alternating current impedance spectroscopy in the range of 0−30 GPa at room temperature, we observed a phase transition at ∼11 GPa, with the conductivity increasing by an order of magnitude. Above ∼20 GPa, $Na_2C_6O_6$ gradually amorphized. During the decompression process, the pressure regulation of the structure and properties of the material are reversible. Our study shows that applying external pressure is an effective tool to improve the conductivity of molecular battery materials. The investigation will help to obtain next-generation electrode materials.

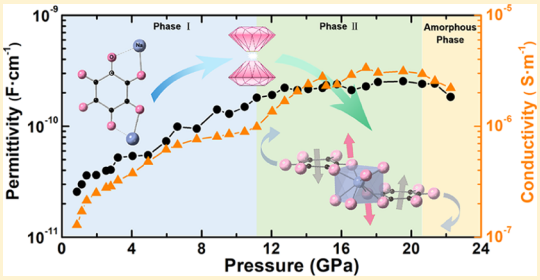

INTRODUCTION

Organic electroactive materials represent a new generation of sustainable energy storage technology because of their unique features including environmental benignity, material sustainability, and highly tailorable properties.[1−4] Among them, polycarbonyl compounds have gradually become a research hotspot of lithium/sodium battery electrode materials because of their high reversible redox reaction, structural diversity, high specific capacity, and fast reaction kinetics.[5,6] These materials often have conjugated structures with multiple carbonyl functional groups ($n \geq 2$), such as quinone and anthraquinone et al.[7] Recently, the carbonyl compounds like $M_2(CO)_5$ and $M_2(CO)_6$ (M = Li, Na, K) with cyclic ketone structure were reported to show excellent cyclic stability and ultrahigh capacity.[8] Cyclohexanehexone (C_6O_6), the prototype with the highest oxidation state, was reported very recently, which exhibits the highest capacity and energy density among all the reported organic cathode materials.[9]

Sodium rhodizonate ($Na_2C_6O_6$, Figure 1), which was a common compound prepared from a natural product, myo-inositol, was evidenced to be a potential cathode of the sodium-ion battery.[10] It provides four Na^+ storage sites during charging and discharging with a theoretical capacity of 501 mA h•g^{-1}. $Na_2C_6O_6$ has alternated layers of pseudo-hexagonally packed Na^+ cations and rhodizonate dianions ($C_6O_6^{2-}$), which is beneficial to the removal and embedding of Na^+ during cycling.[11] Yaqun Wang et al. synthesized the samples of $Na_2C_6O_6$ with different sizes and morphologies, and they found the nanorod exhibits the best performance with a reversible capacity of ∼190 mA h•g^{-1}.[12] Recently, by combining the in situ X-ray diffraction (XRD), it was found that the irreversible phase transition of $Na_2C_6O_6$ during cycling is responsible for deteriorating its redox activity. By modifying

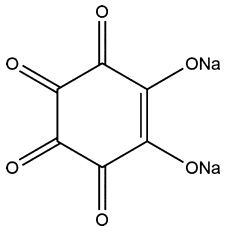

Figure 1. Chemical structure of $Na_2C_6O_6$.

Received: May 15, 2019
Revised: June 14, 2019
Published: June 20, 2019

DOI: 10.1021/acs.jpcc.9b04610
J. Phys. Chem. C 2019, 123, 17163−17169

the particle size and electrolyte conditions, four sodium storages in a $Na_2C_6O_6$ were realized with a capacity of 484 mA h•g^{-1}, which is very close to the theoretical capacity.[13] However, its poor ionic/electronic conductivity limits the application.

Pressure is an effective method to modify the chemical bond and crystal structure, and hence tune the properties of the material.[14−16] Several representative lithium-ion battery materials including the $LiFePO_4$, $LiMn_2O_4$, and Li_2MnSiO_4 were investigated under extreme conditions.[17−19] The lithium titanium oxide ($Li_4Ti_5O_{12}$, LTO), called as "zero-strain" anode materials, shows an order of magnitude enhancement of the conductivity when it amorphizes under high pressure.[20] The amorphous state leading by the different compressibilities of the LiO_6 and TiO_6 octahedra promotes the diffusion of Li^+ ions and increases its ionic conductivity by providing defects for ion migration. The external pressure can also drive the unsaturated bonds like C≡C to polymerize to form the extended framework (pressure-induced polymerization, PIP), which completely changes the structure and hence the conductivity. 10^9-times enhancement of conductivity was observed by compressing lithium acetylide (Li_2C_2), which was previously reported to be a promising electrode material with a capacity of 700 mA h•g^{-1}, but limited by its low conductivity.[21,22] Carbonyl compounds also polymerize under applied pressure. Carbon monoxide (CO), which is recognized as the simplest carbonyl compound, polymerizes under high pressure to form a polymer containing lactonic entities and conjugated C═C bonds.[23−25] Aldehyde also polymerizes into polyethers under compression according to theoretical prediction.[26] Moreover, besides the simple PIP, the pressure induced ring-opening polymerization was observed in the lactide, a more complex compounds containing carbonyl groups, which suggests more possibilities for promising materials under extreme conditions.[27]

Thus, it is worthy to investigate the effect of external pressure on the conductivity and the structural variation of the polycarbonyl electrode materials. In this work, we explored the conductivity of $Na_2C_6O_6$ upon compression using the alternating current impedance spectroscopy. The conductivity increases by an order of magnitude above 11−15 GPa. In situ Raman and infrared (IR) absorption spectra as well as the XRD confirmed the structural phase transition of $Na_2C_6O_6$ at 11 GPa. The corresponding structural variation was studied by Rietveld refinement of the XRD data, and the relationship between structure and electrical properties was discussed. Additionally, a new route to prepare molecular battery materials is proposed.

EXPERIMENTAL SECTION

Experimental Preparation. $Na_2C_6O_6$ was purchased from Maikun Chemical and recrystallized in ethanol before the experiment. No impurities were detected in the crystallized sample according to the X-ray powder diffraction collected on PANalytical Empyrean diffractometer (Cu K_α radiation, λ = 1.5418 Å) (Figure S1). For the in situ Raman, IR spectra, AC impedance spectroscopy, and XRD experiments, fine powder of $Na_2C_6O_6$ was gently ground in an agate mortar for more than 10 min. A symmetric-style diamond anvil cell (DAC) with 300 μm culet diameter diamonds was used for applying pressure. Type-IIa diamond anvils were used for IR experiment to avoid absorption band at 1000−1300 cm^{-1}. T301 stainless steel gaskets were preindented to a thickness of ∼35 μm, and holes with a diameter of 150 μm were drilled at the center of the indentations to serve as the sample chamber. The pressure was calibrated by ruby fluorescence.[28]

In Situ Raman and IR Absorption Spectra Measurements. For the in situ Raman spectra, a piece of sample of 30 × 30 μm^2 was selected and loaded into the sample chamber. Neon was used as a pressure transition medium. The Raman data were collected on a Renishaw Micro-Raman spectroscopy system equipped with a second-harmonic Nd:YAG laser (operating at 532 nm) in a backscattering geometry for excitation and signal collection. For the in situ IR spectra, dried KBr powder was pressed into a disk with ∼20 μm thickness and filled into the sample chamber with an appropriate size. The sample powder was pressed into a slice with ∼10 μm thickness and placed on the KBr disk in the sample chamber. IR experiments were performed on a Bruker VERTEX 70v with HYPERION 2000 microscope. A Globar was used as a conventional source. The spectra were collected in transmission mode in the range of 600−4000 cm^{-1} with a resolution of 4 cm^{-1} through a 20 × 20 μm^2 aperture. The absorption spectra of diamond anvil filled with KBr in the aperture region was used as the background for IR experiment.

In Situ XRD Measurement. A piece of sample with the size of 30 × 30 μm^2 was selected and filled into the sample chamber. Neon was used as a pressure transition medium. The data were collected at the beamline 12.2.2, Advanced Light Source (ALS), Lawrence Berkeley National Lab (LBNL). The wavelength of the incident X-ray was 0.6199 Å. The preliminary data were reduced using the Dioptas program.[29] Lebail fitting and Rietveld refinement were performed by Jana2006.[30]

AC Impedance Spectroscopy Measurement. The technical process of the microcircuit fabrication was reported by previous literature.[31] A panoramic-style DAC with a diamond culet size of 500 μm in diameter was used. T301 stainless steel gasket was preindented to ∼45 μm thickness, and a hole with a diameter of ∼280 μm was drilled at the indentation center. A mixture of c-BN powder and epoxy was used for the insulation between the platinum electrode and metallic gasket. Two thin platinum foils with a width of ∼300 μm were fixed on the two diamond culets, respectively, to act as electrodes. No pressure transition medium was used. Data were collected using Solartron 1260 impedance analyzer and Solartron 1296 dielectric interface. The AC voltage (100 mV) was applied in the frequency range between 0.1 Hz and 32 MHz. Z-view was used to fit the impedance semicircle to obtain the equivalent circuit diagram and the capacitance.

Computational Details. For the calculation of IR and Raman spectra of $Na_2C_6O_6$ at ambient pressure, our density functional theory (DFT) calculations were performed within generalized gradient approximation (GGA) implemented in the CASTEP module of Material Studio.[32−34] The IR and Raman parameters were calculated using norm-conserving pseudopotentials with an energy cutoff for the plane-wave basis set at 990 eV and k-point sampling less than 0.03 × 2π•A^{-1}.[35,36]

RESULTS AND DISCUSSION

Electrical Conductivity under High Pressure. $Na_2C_6O_6$ is a mixed electronic/ionic conductor. The migration of Na^+ contributes to the electrical conductivity. We measured in situ AC impedance spectroscopy of $Na_2C_6O_6$ up to ∼22 GPa. The Nyquist representations of the impedance spectroscopy of

DOI: 10.1021/acs.jpcc.9b04610
J. Phys. Chem. C 2019, 123, 17163−17169

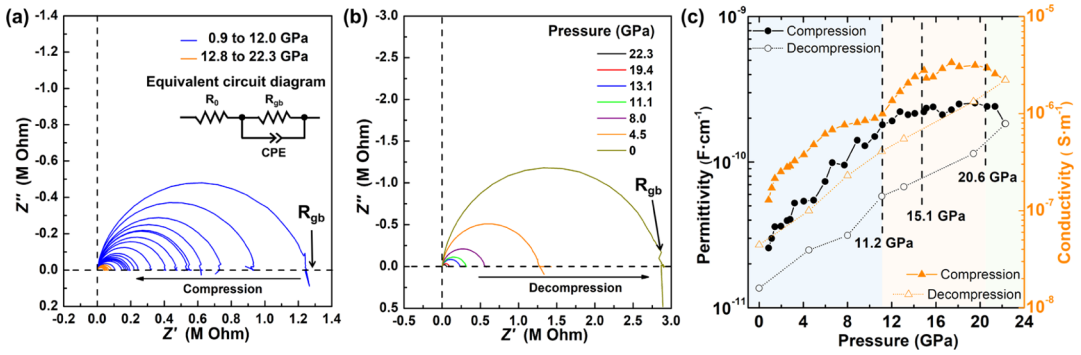

Figure 2. Impedance spectroscopy of $Na_2C_6O_6$ in Nyquist plot under (a) compression and (b) decompression, and the equivalent circuit diagram is shown in the inset. (c) Evolution of the conductivity and permittivity of $Na_2C_6O_6$ with pressures.

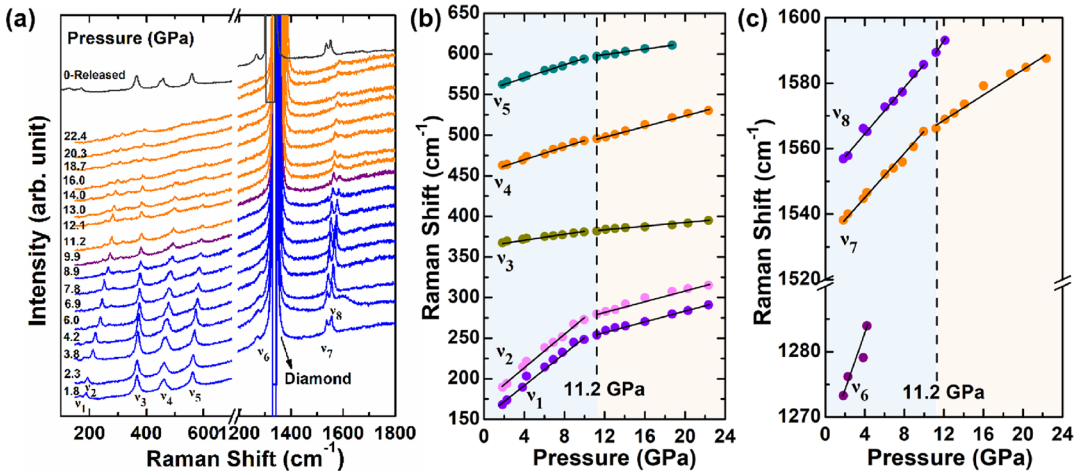

Figure 3. (a) Raman spectra of $Na_2C_6O_6$ in the pressure range of 1.8−22.4 GPa. The "0-Released" indicates the spectrum released from 22.4 GPa. Frequency shifts as a function of pressure ranging from (b) 150 to 650 cm^{-1}, and (c) 1270 to 1600 cm^{-1}.

$Na_2C_6O_6$ during compression and decompression processes are shown in Figure 2a,b, respectively. It shows a single semicircle and no straight line is observed in the low-frequency region, indicating no diffusion of Na^+ into the electrode and no electrochemical reaction happened. For a mixed electronic/ionic conductor, ionic and electronic conductivity can be extracted from the Nyquist plot. With blocking electrodes, the conducting ions (Na^+) cannot go through the electrode/sample interface. Hence, the conductivity is mainly attributed by the electronic conduction (with the resistance R_e) at the low-frequency limit and to the parallel connection of electronic conduction (resistance R_e) and ionic conduction (resistance R_i) at the high-frequency limit, with $R = R_eR_i/(R_e + R_i)$.[37,38] As shown in the Nyquist plot in Figure 2a,b, at the high-frequency end of the semicircle, the resistance is much smaller than that at the low-frequency limit (R_e, approximately equaling to R_{gb}, the grain boundary resistance as discussed below), which means the resistance of the sample is mainly contributed by R_e. Here, we mainly discuss the electronic transport.

Using the Z-view to fit the Nyquist plot, the resistance (R) and capacitance (C) values were obtained. A typical fitting result of Nyquist plot of $Na_2C_6O_6$ at 12.7 GPa is shown in Figure S2. The electrode used in the experiment covered the chamber completely, and the chamber is fulfilled by the sample, so the geometric factors (the diameter and the thickness) of the chamber represent that of the sample. During the compression, the chamber was compressed with the diameter changing from 280 to 235 μm and the thickness changing from 45 to 30 μm. Supposing a linear interpolation algorithm for the geometric factors, the conductivity (σ) and permittivity (ε) in the whole pressure range were calculated by the formulas $\sigma = l/RS$ and $\varepsilon = Cl/S$, where l and S represent the thickness and cross-sectional area of the sample chamber, respectively.

As shown in Figure 2c, the permittivity is in the range of 10^{-9} to 10^{-11} F•cm^{-1}, which suggests that the semicircle corresponds to the impedance of the grain boundary.[39,40] The grain boundary resistance R_{gb} gradually decreases as the pressure increases. This shows that electrons are easier to overcome the grain boundaries under high pressure. An abrupt increase in conductivity is observed in the range of 11.2−15.1 GPa. After that, the conductivity almost keeps constant. At 15.1 GPa, the conductivity is increased by an order of magnitude when compared to that at ambient pressure. Above 20.6 GPa, there is a declining trend. In the progress of decompression, the conductivity gradually decreases. According to the variation, it is proved that the electrical properties of the material are significantly affected by the pressure, and the pressure-induced transitions that happened at 11.2 and 20.6 GPa. To understand the structural origin, the in situ Raman, IR spectra, and XRD under high pressure were employed to investigate the variations of intermolecular interactions and molecular aggregations.

Raman and IR Spectra under High Pressure. The evolution of the Raman spectra of $Na_2C_6O_6$ up to 22.4 GPa is shown in Figure 3a. Table 1 is the assignments of the Raman

DOI: 10.1021/acs.jpcc.9b04610
J. Phys. Chem. C 2019, 123, 17163−17169

Table 1. Assignments of Raman Modes of $Na_2C_6O_6$ at 1.8 GPa

Mode	frequencies (cm^{-1}) experiment (1.5 GPa)	frequencies (cm^{-1}) calculation (ambient pressure)	assignments
ν_1	168	154	CO out of plane bending
ν_2	189	176	CO out of plane bending
ν_3	366	353	CO in-plane bending
ν_4	461	449	CO out of plane bending
ν_5	563	544	ring breathing
ν_6	1270	1273	CC stretching
ν_7	1535	1522	CO stretching
ν_8	1556	1571	CO stretching

modes at 1.8 GPa. During compression, all the Raman peaks significantly blue-shifted because of the decreasing interatomic distances and the enhancement of the interatomic interaction. At 11.2 GPa, the ν_1, ν_2, ν_7, and ν_8 modes show obvious discontinuities (Figure 3b,c). This indicates a phase transition at ~11 GPa. Upon further compression, the peaks were broadened and weakened. Above 20 GPa, all the Raman peaks disappeared, suggesting that the sample turned into an amorphous state. Under decompression, the peaks appeared again (Figure S3), and the Raman spectra of the recovered sample was the same as that at ambient pressure (Figure 3a), which suggests that the phase transitions (or if any chemical reactions) of $Na_2C_6O_6$ up to 22.4 GPa are reversible.

In situ IR spectra between 600 and 2800 cm^{-1} were collected from 1.5 to 40.7 GPa (Figure 4a). The assignments of the IR modes at 1.5 GPa were shown in Table 2. Besides the expected blue-shift up to 40.7 GPa, an obvious discontinuity was observed in the peak of the combination band at ~2600 cm^{-1} ($\nu_{10} + \nu_{11}$) and it shows slight red shift above 11.8 GPa (Figure 4b). This result also demonstrates the minor phase transition that happened at around 11 GPa, consistent with the Raman results. The IR spectra of $Na_2C_6O_6$ recovered from 40 GPa is consistent with that before compression (Figure 4a and S4), which also demonstrates that the phase transition at 11 GPa is reversible and the carbon skeleton with six-membered ring and carbonyl group of the sample were not destroyed under high pressure.

From the Raman and the IR spectra, we conclude that the phase transition of $Na_2C_6O_6$ happened around 11 GPa, and the amorphization is around 20 GPa, which is the origin of the transitions observed in the AC impedance experiment. The amorphization of $Na_2C_6O_6$ provides a reasonable explanation for the decrease of conductivity and permittivity under high pressure.

XRD under High Pressure. In order to understand the enhancement of conductivity of $Na_2C_6O_6$ under high pressure and its phase-transition mechanism, we performed in situ XRD measurements to investigate its structure evolution under compression. The diffraction patterns during compression are shown in Figure 5. At ambient pressure, the $Na_2C_6O_6$ crystallized into the orthorhombic phase (space group *Fddd*). Under high pressure, most peaks moved toward low *d*-spacing, indicating the compression of the lattice. Several peaks were broadened first and then disappeared gradually at 22.8 GPa, indicating that the sample transforms into an amorphous state. The lattice constants of $Na_2C_6O_6$ at various pressures were

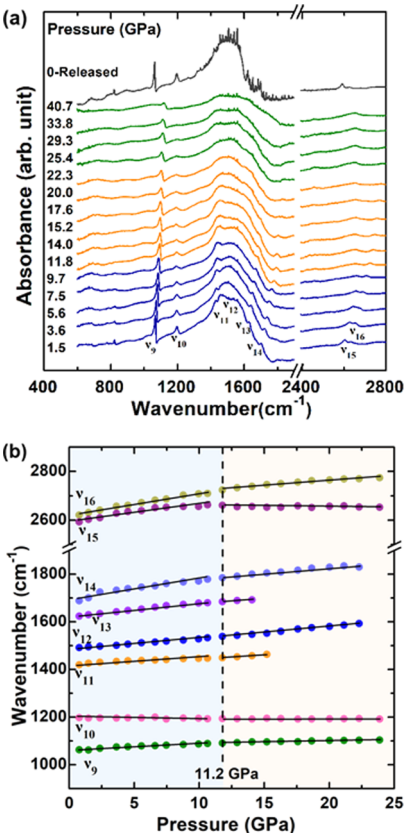

Figure 4. (a) In situ IR spectra of $Na_2C_6O_6$ in the pressure range of 1.5−40.7 GPa. The "0-Released" indicates the spectrum released from 40.7 GPa. (b) The pressure dependence of selected IR absorption peaks.

obtained by performing the Rietveld refinement and shown in Figure 6a. An obvious discontinuity was observed at 11.8 GPa. The relationship between pressure and unit cell volume was plotted and fitted by the 3rd order Birch−Murnaghan equation of state (B−M EOS)

$$P(V) = \frac{3}{2}B_0\left[\left(\frac{V_0}{V}\right)^{7/3} - \left(\frac{V_0}{V}\right)^{5/3}\right]\left\{1 + \frac{3}{4}(B_1 - 4)\left[\left(\frac{V_0}{V}\right)^{2/3} - 1\right]\right\}$$

B_0 and B_1 are ambient bulk modulus and its derivative, respectively, and V_0 is the unit cell volume at ambient conditions. As shown in Figure 6b, there is a discontinuity at ~12 GPa. Thus, two curves were chosen to fit the data, respectively. In the range of 0.8−11.8 GPa, V_0 obtained by fitting is 1304.0 ± 5.2 Å^3, which is almost consistent with the actual unit cell volume. The B_0 and B_1 are 23.6 ± 1.7 GPa, and 5.6 ± 0.5, respectively. In the range of 13.1−19.7 GPa, V_0 = 1162.7 ± 8.5 Å^3, B_0 = 70.4 ± 4.2 GPa, and B_1 is fixed to 4. The V_0 is much smaller than that below 12 GPa, while the bulk modulus is significantly larger. This means the sample is much more difficult to be compressed, which clearly demonstrated the phase transition, and is consistent with the results shown above.

To understand the variation of the crystal structure under applied pressure, we performed Rietveld refinement on the in situ XRD patterns. The plots of 10.6 and 11.8 GPa are shown

DOI: 10.1021/acs.jpcc.9b04610
J. Phys. Chem. C 2019, 123, 17163−17169

Table 2. Assignments of IR Modes of $Na_2C_6O_6$ at 1.5 GPa

Mode	frequencies (cm^{-1}) experiment (1.5 GPa)	calculation (ambient pressure)	references[41,42] (ambient pressure)	assignments
ν_9	1062	1046	1058	CC stretching
ν_{10}	1196	1241	1252	CC stretching
ν_{11}	1425	1430	1449	CO stretching
ν_{12}	1495	1460	1465	CO stretching
ν_{13}	1628	1517	1546	CO stretching
ν_{14}	1699	1561	1669	CO stretching
ν_{15}	2603			$\nu_{10} + \nu_{11}$
ν_{16}	2631			$\nu_{10} + \nu_{12}$

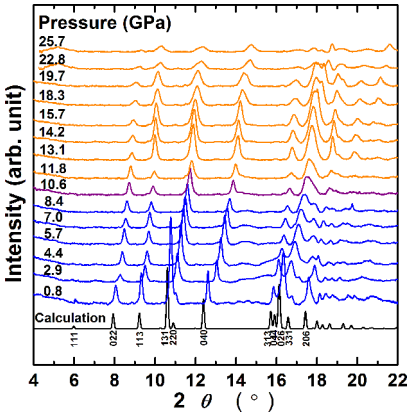

Figure 5. In situ synchrotron XRD patterns of $Na_2C_6O_6$ in the pressure range of 0.8−25.7 GPa.

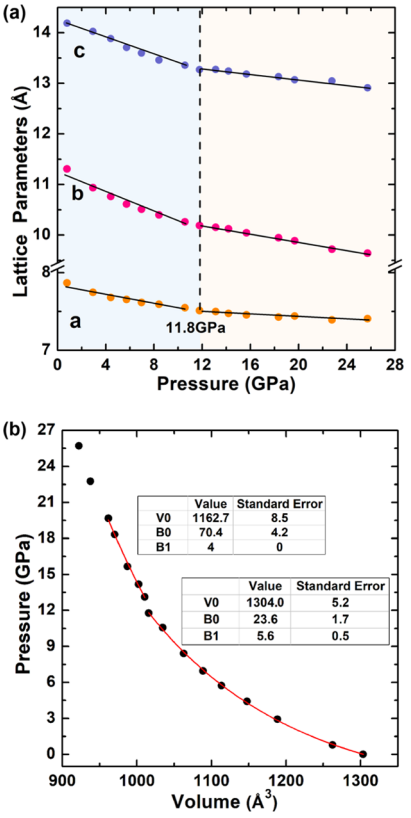

Figure 6. (a) Variations in lattice parameters of $Na_2C_6O_6$ as a function of pressure. (b) Pressure dependence of the unit cell volume of $Na_2C_6O_6$. The solid lines represent the fitting results of the 3rd order B−M EOS in the pressure range of 0.8−19.7 GPa. The insets show the fitting results of V_0, B_0, and B_1 of these two phases.

in Figure S5. At ambient pressure, the layers of rhodizonate dianions ($C_6O_6^{2-}$) are perpendicular to *b*-axis and alternately stacked with sodium cation (Na^+) layers (Figure 7a). Each Na^+ is coordinated by eight oxygen atoms from four different rhodizonate anions, two anions from the *a* and *-a* directions on the upper (lower) layer, and the other two anions from the ±*a* ±*c* directions on the lower (upper) layer, with each anion contributing two oxygen atoms. A square antiprism is hence formed, thereby separating adjacent $C_6O_6^{2-}$ in the structure. Under compression, the distance between the Na^+ and the nearest $C_6O_6^{2-}$ layer increased (Figure 7b), the Na^+ moved toward the center between the $C_6O_6^{2-}$ layers, and the antiprism becomes more symmetrical. Above 10.6 GPa, this distance suddenly became smaller, and continued to decrease as the pressure increases. The antiprism became unsymmetrical again. Additionally, a sudden increase of the distance between Na^+ and O2 was observed at 11.8 GPa. Comparing the local structure of 10.6 and 11.8 GPa (Figure 7c), we found that the C−O2 bond is deflected to the *-b*-axis, causing the sudden increase of Na−O2 length and the deformation of Na−O square antiprism, which is the structural origin of the phase transition.

Based on the crystal structure, we can find the conductive anions are separated by Na−O ionic bonds and intermolecular repulsion. The approaching of the neighbored $C_6O_6^{2-}$ to each other under compression is the key reason for the enhancement of the conductivity before the phase transition, while the abrupt deformation of the NaO_8 antiprism is responsible for the phase transition and hence the abrupt increasing of the conductivity. After the phase transition, the material is much more difficult to be compressed, and the Na−O polyhedron is hindering the approach between the anions and hence the electronic conduction. This is the bottle-neck for the electronic conduction.

To further improve the electronic conductivity of $Na_2C_6O_6$, it would be helpful to chemically bond the anions and form extended conjugated structures. A feasible method is to introduce polymerizable functional groups such as alkynyl. If carbonyl compounds can be compressed to polymerize and be recovered to ambient pressure, the conductivity can be improved effectively. Smaller cations like Li^+ may also help to change the M−O coordination and improve the packing efficiency. Additionally, besides the modification of the crystal structure, the grain size should also be considered. Obtaining nanoscale materials may be a way to modify the grain boundary and thus increase its conductivity.

DOI: 10.1021/acs.jpcc.9b04610
J. Phys. Chem. C 2019, 123, 17163−17169

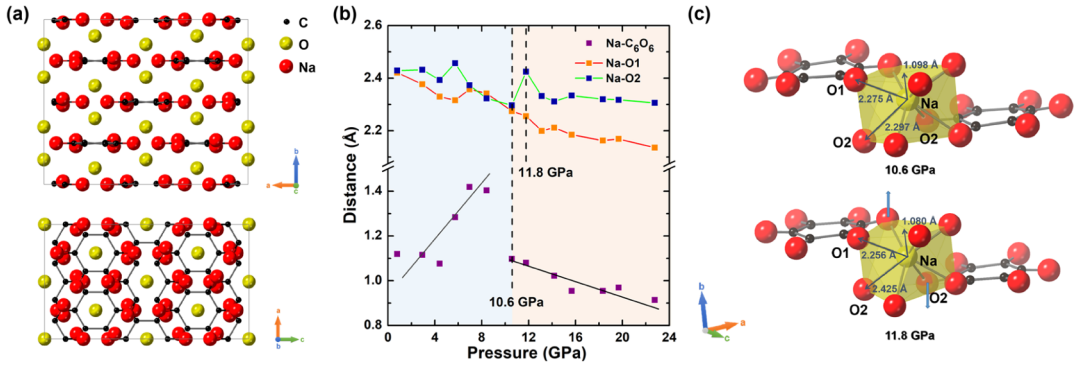

Figure 7. (a) Crystal structure of $Na_2C_6O_6$ at ambient pressure. (b) Distance in the *b*-axis direction between the Na^+ and the $C_6O_6^{2-}$ layer, the evolution of bond length between Na^+ and O1 and O2 with pressure. (c) Crystal structures of $Na_2C_6O_6$ at 10.6 and 11.8 GPa. The arrows indicate the movement direction of O2.

CONCLUSIONS

In conclusion, the structural evolution process of $Na_2C_6O_6$ upon compression and the relationship between electrical properties and structures were investigated by in situ Raman and IR spectra as well as XRD. At about 11 GPa, the Na−O coordination square antiprism geometry deformed significantly, resulting in a structural phase transition. After that, the conductivity of $Na_2C_6O_6$ increase by an order of magnitude. When the pressure was further increased to 20 GPa, the deformation of the crystal lattice gradually caused the structure of the molecular skeleton to collapse, resulting in an amorphous state, and the electronic conductivity gradually decreases. These findings provide new ideas for improving the conductivity of $Na_2C_6O_6$, and also prove that high-pressure technology is an effective method to regulate the structure and electrical properties of materials.

ASSOCIATED CONTENT

Supporting Information

The Supporting Information is available free of charge on the ACS Publications website at DOI: 10.1021/acs.jpcc.9b04610.

The XRD pattern of recrystallized $Na_2C_6O_6$ powder; selected fitting of the Nyquist plot of $Na_2C_6O_6$ at 12.7 GPa; In situ Raman and IR spectra of $Na_2C_6O_6$ during decompression; and Rietveld refinement results of $Na_2C_6O_6$ at 10.6 and 11.8 GPa (PDF)

AUTHOR INFORMATION

Corresponding Authors

*E-mail: likuo@hpstar.ac.cn (K.L.).
*E-mail: zhenghy@hpstar.ac.cn (H.Z.).

ORCID

Kuo Li: 0000-0002-4859-6099
Haiyan Zheng: 0000-0002-4727-5912

Author Contributions

The manuscript was written through contributions of all authors. All authors have given approval to the final version of the manuscript.

Notes

The authors declare no competing financial interest.

ACKNOWLEDGMENTS

The authors acknowledge the support of the National Natural Science Foundation of China (NSFC) (grant nos. 21771011, 21601007 and 21875006). The authors also acknowledge the support from the Top 1000-Talents Award. This research used resources of the Advanced Light Source, which is a DOE Office of Science User Facility under contract no. DE-ac02-05CH11231. The authors thank Dr. Hyun Hwi Lee for the help on the in situ XRD experiment at X-ray Scattering Beamline for Materials Science (5A XRS-MS) beamline of the Pohang Light Source (PLS-II) at Pohang Accelerator Laboratory (PAL), Korea. The authors thank Dr. Saori Kawaguchi for the help on the in situ XRD experiment at BL 10XU, SPring-8, Japan. Xiao Dong thanks the support of NSFC (No. 21803033) and Yong Elite Scientists Sponsorship Program by Tianjin (No. TJSQNTJ-2018-18).

REFERENCES

(1) Armand, M.; Tarascon, J.-M. Building Better Batteries. *Nature* **2008**, *451*, 652−657.
(2) Larcher, D.; Tarascon, J.-M. Towards Greener and More Sustainable Batteries for Electrical Energy Storage. *Nat. Chem.* **2015**, *7*, 19−29.
(3) Song, Z.; Zhou, H. Towards Sustainable and Versatile Energy Storage Devices: An Overview of Organic Electrode Materials. *Energy Environ. Sci.* **2013**, *6*, 2280−2301.
(4) Muench, S.; Wild, A.; Friebe, C.; Häupler, B.; Janoschka, T.; Schubert, U. S. Polymer-Based Organic Batteries. *Chem. Rev.* **2016**, *116*, 9438−9484.
(5) Häupler, B.; Wild, A.; Schubert, U. S. Carbonyls: Powerful Organic Materials for Secondary Batteries. *Adv. Energy Mater.* **2015**, *5*, 14020434.
(6) Zhu, Z.; Hong, M.; Guo, D.; Shi, J.; Tao, Z.; Chen, J. All-Solid-State Lithium Organic Battery with Composite Polymer Electrolyte and Pillar[5]quinone Cathode. *J. Am. Chem. Soc.* **2014**, *136*, 16461−16464.
(7) Liang, Y.; Zhang, P.; Chen, J. Function-Oriented Design of Conjugated Carbonyl Compound Electrodes for High Energy Lithium Batteries. *Chem. Sci.* **2013**, *4*, 1330−1337.
(8) Zhao, Q.; Wang, J.; Lu, Y.; Li, Y.; Liang, G.; Chen, J. Oxocarbon Salts for Fast Rechargeable Batteries. *Angew. Chem., Int. Ed. Engl.* **2016**, *55*, 12528−12532.
(9) Lu, Y.; Hou, X.; Miao, L.; Li, L.; Shi, R.; Liu, L.; Chen, J. Cyclohexanehexone with Ultrahigh Capacity as Cathode Materials for Lithium-Ion Batteries. *Angew. Chem., Int. Ed. Engl.* **2019**, *58*, 7020.
(10) Chihara, K.; Chujo, N.; Kitajou, A.; Okada, S. Cathode Properties of $Na_2C_6O_6$ for Sodium-Ion Batteries. *Electrochim. Acta* **2013**, *110*, 240−246.
(11) Dinnebier, R. E.; Nuss, H.; Jansen, M. Disodium Rhodizonate: a Powder Diffraction Study. *Acta Crystallogr., Sect. E: Struct. Rep. Online* **2010**, *61*, 2148−2150.

DOI: 10.1021/acs.jpcc.9b04610
J. Phys. Chem. C 2019, 123, 17163−17169

(12) Wang, Y.; Ding, Y.; Pan, L.; Shi, Y.; Yue, Z.; Shi, Y.; Yu, G. Understanding the Size-Dependent Sodium Storage Properties of $Na_2C_6O_6$-Based Organic Electrodes for Sodium-Ion Batteries. *Nano Lett.* **2016**, *16*, 3329−3334.
(13) Lee, M.; Hong, J.; Lopez, J.; Sun, Y.; Feng, D.; Lim, K.; Chueh, W. C.; Toney, M. F.; Cui, Y.; Bao, Z. High-Performance Sodium-Organic Battery by Realizing Four-Sodium Storage in Disodium Rhodizonate. *Nat. Energy.* **2017**, *2*, 861−868.
(14) Mao, H.-K.; Chen, B.; Chen, J.; Li, K.; Lin, J.-F.; Yang, W.; Zheng, H. Recent Advances in High-Pressure Science and Technology. *Matter Radiat. Extremes* **2016**, *1*, 59−75.
(15) Mao, H.-K.; Chen, X. J.; Ding, Y.; Li, B.; Wang, L. Solids, Liquids, and Gases under High Pressure. *Rev. Mod. Phys.* **2018**, *90*, 015007.
(16) Wang, X.; Zhang, P.; Li, K.; Zheng, H. Chemical Reactions of Molecules under High Pressure. *Chemistry* **2019**, *82*, 387−398.
(17) Dong, H.; Guo, H.; He, Y.; Gao, J.; Han, W.; Lu, X.; Yan, S.; Yang, K.; Li, H.; Chen, D.; et al. Structural Stability and Li-Ion Transport Property of $LiFePO_4$ under High-Pressure. *Solid State Ionics* **2017**, *301*, 133−137.
(18) Yamaura, K.; Huang, Q.; Zhang, L.; Takada, K.; Baba, Y.; Nagai, T.; Matsui, Y.; Kosuda, K.; Takayama-Muromachi, E. Spinel-to-$CaFe_2O_4$-Type Structural Transformation in $LiMn_2O_4$ under High Pressure. *J. Am. Chem. Soc.* **2006**, *128*, 9448−9456.
(19) Santamaría-Pérez, D.; Amador, U.; Tortajada, J.; Dominko, R.; Arroyo- de Dompablo, M. E. High-Pressure Investigation of Li_2MnSiO_4 and Li_2CoSiO_4 Electrode Materials for Lithium-Ion Batteries. *Inorg. Chem.* **2012**, *51*, 5779−5786.
(20) Huang, Y.; He, Y.; Sheng, H.; Lu, X.; Dong, H.; Samanta, S.; Dong, H.; Li, X.; Kim, D. Y.; Mao, H.-K.; et al. Li-Ion Battery Material under High Pressure: Amorphization and Enhanced Conductivity of $Li_4Ti_5O_{12}$. *Natl. Sci. Rev.* **2018**, *6*, 239.
(21) Tian, N.; Gao, Y.; Li, Y.; Wang, Z.; Song, X.; Chen, L. Li_2C_2, a High-Capacity Cathode Material for Lithium Ion Batteries. *Angew. Chem., Int. Ed. Engl.* **2016**, *55*, 644−648.
(22) Wang, L.; Dong, X.; Wang, Y.; Zheng, H.; Li, K.; Peng, X.; Mao, H.-k.; Jin, C.; Meng, Y.; Huang, M.; et al. Pressure-Induced Polymerization and Disproportionation of Li_2C_2 Accompanied with Irreversible Conductivity Enhancement. *J. Phys. Chem. Lett.* **2017**, *8*, 4241−4245.
(23) Yoo, C.-S.; Kim, M.; Lim, J.; Ryu, Y. J.; Batyrev, I. G. Copolymerization of CO and N_2 to Extended CO-N_2 Framework Solid at High Pressures. *J. Phys. Chem. C* **2018**, *122*, 13054−13060.
(24) Rademacher, N.; Bayarjargal, L.; Morgenroth, W.; Winkler, B.; Jennifer, C. K.; Batyrev, I. G.; Milman, V. The Local Atomic Structures of Liquid CO at 3.6 GPa and Polymerized CO at 0 to 30 GPa from High-Pressure Pair Distribution Function Analysis. *Chem.—Eur. J.* **2015**, *20*, 11531−11539.
(25) Ryu, Y.-J.; Yoo, C.-S.; Kim, M.; Yong, X.; Tse, J.; Lee, S. K.; Kim, E. J. Hydrogen-Doped Polymeric Carbon Monoxide at High Pressure. *J. Phys. Chem. C* **2017**, *121*, 10078−10086.
(26) Venkateswaran, S.; Bhagavantam, S. The Raman Spectra of some Aldehydes and of Mesitylene. *Proc. R. Soc. A* **1930**, *128*, 252−262.
(27) Ceppatelli, M.; Frediani, M.; Bini, R. High-Pressure Reactivity of l, l-Lactide. *J. Phys. Chem. B* **2011**, *115*, 2173−2184.
(28) Mao, H. K.; Xu, J.; Bell, P. M. Calibration of the Ruby Pressure Gauge to 800 kbar under Quasi-Hydrostatic Conditions. *J. Geophys. Res.* **1986**, *91*, 4673−4676.
(29) Prescher, C.; Prakapenka, V. B. A Program for Reduction of Two-Dimensional X-ray Diffraction Data and Data Exploration. *High Pressure Res.* **2015**, *35*, 285−288.
(30) Petříček, V.; Dušek, M.; Palatinus, L. Crystallographic Computing System JANA2006: General Features. *Z. Kristallogr.—Cryst. Mater.* **2014**, *229*, 345−352.
(31) Hu, T.; Cui, X.; Gao, Y.; Han, Y.; Liu, C.; Liu, B.; Liu, H.; Ma, Y.; Gao, C. In situ Hall Effect Measurement on Diamond Anvil Cell under High Pressure. *Rev. Sci. Instrum.* **2010**, *81*, 115101.
(32) Perdew, J. P.; Chevary, J. A.; Vosko, S. H.; Jackson, K. A.; Pederson, M. R.; Singh, D. J.; Fiolhais, C. Atoms, Molecules, Solids, and Surfaces: Applications of the Generalized Gradient Approximation for Exchange and Correlation. *Phys. Rev. B: Condens. Matter Mater. Phys.* **1992**, *46*, 6671−6687.
(33) Juan, Y.-M.; Kaxiras, E.; Gordon, R. G. Use of the Generalized Gradient Approximation in Pseudopotential Calculations of Solids. *Phys. Rev. B: Condens. Matter Mater. Phys.* **1995**, *51*, 9521−9525.
(34) Clark, S. J.; Segall, M. D.; Pickard, C. J.; Hasnip, P. J.; Probert, M. J.; Refson, K.; Payne, M. C. Z. First Principles Methods Using CASTEP. *Z. für Kristallogr.—Cryst. Mater.* **2005**, *220*, 567−570.
(35) Baroni, S.; de Gironcoli, S.; Dal Corso, A.; Giannozzi, P. Phonons and Related Crystal Properties from Density-Functional Perturbation Theory. *Rev. Mod. Phys.* **2001**, *73*, 515−562.
(36) Porezag, D.; Pederson, M. R. Infrared Intensities and Raman-Scattering Activities within Density-Functional Theory. *Phys. Rev. B: Condens. Matter Mater. Phys.* **1996**, *54*, 7830.
(37) Wang, C.; Hong, J. Ionic/Electronic Conducting Characteristics of $LiFePO_4$ Cathode Materials. The Determining Factors for High Rate Performance. *Electrochem. Solid-State Lett.* **2007**, *10*, A65.
(38) Jamnik, J. Impedance Spectroscopy of Mixed Conductors with Semi-Blocking Boundaries. *Solid State Ionics* **2003**, *157*, 19−28.
(39) Sinclair, D. C. Characterization of Electro-Materials Using AC Impedance Spectroscopy. *Bol. Soc. Esp. Ceram. Vidrio* **1995**, *65*, 55−66.
(40) Irvine, J. T. S.; Sinclair, D. C.; West, A. R. Electroceramics: Characterization by Impedance Spectroscopy. *Adv. Mater.* **1990**, *2*, 132−138.
(41) Junqueira, G. M. A.; Rocha, W. R.; De Almeida, W. B.; Dos Santos, H. F. Theoretical Study of Oxocarbons: Structure and Vibrational Spectrum of the D_{6h} and C_2 Forms of the Rhodizonate Ion. *J. Mol. Struct.: THEOCHEM* **2004**, *684*, 141−147.
(42) Bailey, R. T. Vibrational Spectra and Structure of the Rhodizonate Dianion. *J. Chem. Soc. B.* **1971**, 627−629.

DOI: 10.1021/acs.jpcc.9b04610
J. Phys. Chem. C 2019, 123, 17163−17169